Electronic and Thermal Transport Properties of Nanostructured Thermoelectric Materials Sintered from Chemically Synthesized Tin Sulfide Nanoparticles and Effects of Ag and Se Doping

Keiji Kobayashi,[1] Mari Takahashi,[1] Simon Moore,[1] Masanobu Miyata,[1] Philipp Sauerschnig,[2] Jun Uzuhashi,[3] Michihiro Ohta,[2] Tadakatsu Ohkubo,[3] and Shinya Maenosono[1]*

[1] School of Materials Science, Japan Advanced Institute of Science and Technology, 1-1 Asahidai, Nomi, Ishikawa 923-1292, Japan

[2] Global Zero Emission Research Center , National Institute of Advanced Industrial Science and Technology (AIST), Tsukuba, Ibaraki 305-8569, Japan

[3] Research Center for Magnetic and Spintronic Materials, National Institute for Materials Science (NIMS), 1-2-1 Sengen, Tsukuba, Ibaraki 305-0047, Japan

Corresponding Author

*E-mail: shinya@jaist.ac.jp.

KEYWORDS: Thermoelectric materials, Sulfide, Nanoparticles, Phonon scattering, Carrier scattering, Effective mass

ABSTRACT

To shine light on the mechanisms involved in the doping of the sustainable thermoelectric material SnS with Ag and Se, we present a detailed investigation into Ag and Se-doped SnS nanoparticles (NPs). SnS NPs, Ag-doped SnS NPs and Ag-doped $SnS_{1-x}Se_x$ NPs were chemically synthesized and sintered into pellets by hot-pressing. The structure, thermoelectric, electronic and thermal transport properties were then investigated using a variety of techniques. As a result, it was found that when Ag-doped SnS NPs were sintered, two types of Ag were present in the sintered pellets: one in the form of segregated Ag-rich nanoprecipitates, and the other in the form of interlayer intercalated Ag ions. In contrast, when Ag-doped $SnS_{1-x}Se_x$ NPs were sintered, Se was found to form a homogeneous solid solution. The effects of these three impurity-derived structures on the electronic and thermal transport properties were investigated. The final *ZT* values for SnS doped with 1.5 at% Ag (SnS:Ag) and $SnS_{0.9}Se_{0.1}$:Ag, in which SnS:Ag was further doped with Se, were 0.09 at 666 K and 0.14 at 667 K, respectively.

INTRODUCTION

Tin monochalcogenides SnE (E = S, Se, Te) have attracted much attention as semiconductors with good optical properties for photovoltaics, photodetectors, and other electronic devices.[1-3] Of these, SnS and SnSe are layered materials with accordion-like zigzag structures. SnSe has also attracted a great deal of attention as a high-performance thermoelectric material due to its high phonon anharmonicity and extremely low lattice thermal conductivity, κ_l.[4,5] Since SnS has a crystal structure similar to that of SnSe, and S is less toxic than Se and more abundant than Te, SnS has the potential to be an effective, environmentally friendly thermoelectric material. The replacement of Se and Te with S has been done not only with Sn-S but also with Cu-S and Pb-S materials. Using materials with similar structures helps in the development and understanding of the strategy for the optimization of their electrical and thermal transport properties.[6] However, the reported thermoelectric properties of SnS, which are represented by the dimensionless figure of merit, ZT ($ZT = \sigma S^2/\kappa$ where σ, S and κ are the electrical conductivity, Seebeck coefficient and thermal conductivity, respectively), is quite low compared to SnSe and SnTe. Reported values of ZT at 650 K are approximately 0.01 along the in-plane direction of the pellet (perpendicular to the pressing direction) for SnS,[7] compared with 0.44 along the b axis for SnSe,[4] and 0.17 along the out-of-plane direction of the pellet (parallel to the pressing direction) for SnTe.[8] This is due to the higher κ_l and lower power factor, PF ($= \sigma S^2$), of SnS (κ_l = 0.77 $W \cdot m^{-1} \cdot K^{-1}$ and PF = 0.17 $\mu W \cdot cm^{-1} \cdot K^{-2}$ along the in-plane direction at 650K)[7] than SnSe (κ_l = 0.36 $W \cdot m^{-1} \cdot K^{-1}$ and PF = 2.54 $\mu W \cdot cm^{-1} \cdot K^{-2}$ along the b axis at 650K)[4]. Therefore, SnS cannot currently replace SnSe or SnTe as a potential practical thermoelectric material.

However, SnSe and SnTe are limited in their practical application due to the high toxicity of Se and the low abundance of Te, whereas SnS is a much more sustainable material with promise

for improvement. There are many reports on the *ZT* enhancement of SnSe and SnTe by multiple methods, (e. g., lattice plainification[9] and SnO_x removal[10] for SnSe, and band engineering[11] and nanocomposites fabrication[12] for SnTe), but relatively few on SnS, with those that exist focusing on impurity doping meaning that the improvement of *ZT* in SnS is ongoing. For example, Tan *et al.* prepared Ag-doped SnS by mixing Sn, S, and Ag powders using a mechanical alloying method for 15 h followed by spark plasma sintering (SPS) at 933 K for 5 min. They succeeded in increasing the Hall carrier concentration n_H up to 3.6×10^{18} cm^{-3} and improved *ZT* to about 0.13 at 673 K (maximum *ZT* was 0.6 at 923 K) for the sample with a doping level of 0.5 at% Ag.[13] Zhou *et al.* prepared Na-doped SnS using a hot-melting method. Sn, S and Na sources were heated at 1193 K for 4 h and annealed at 923 K for 3 days. The obtained ingots were then crushed into powders, followed by pelletization by hot press at 823 K under a pressure of ~80 MPa for 30 min. The n_H was significantly increased up to 2.0×10^{19} cm^{-3} by Na acting as an acceptor and the *ZT* value at 675 K was about 0.3 for the sample with a doping level of 2 at% Na (maximum *ZT* was 0.65 at 850 K).[14] He *et al.* prepared Na and Se co-doped SnS ingots using a temperature gradient method, which were then crushed, melted and heat-treated for 10 h at 1313 K. After cooling, the obtained ingots were cut into multiple pieces of different shapes and sizes for properties measurement and evaluation. The *ZT* value at 673 K was about 1.4 for the sample co-doped with 2 at% Na and 9 at% Se (maximum *ZT* was 1.6 at 873 K).[15] This was a result of the higher n_H again due to Na doping as an acceptor, and the partial substitution of S with Se, resulting in a lower κ_l than SnS. In a similar example, He *et al.* made Ag and Se co-doped SnS using a vacuum hot-melting method. Sn, S, Ag, and Se sources were heated at 873 K for 30 h and then at 1223 K for 6 h. The obtained ingots were crushed into powders, and pelletized by a hot press at 873 K under a pressure of ~50 MPa for 10 min. In contrast with the other reports, a *ZT* of about 0.15 around 670 K (maximum

ZT of 0.8 at 873 K) was achieved with doping levels of 2 at% Ag and only 1 at% Se, which showed a significant increase of n_H due to Ag acting as an acceptor, and a reduction in κ_l through the substitution of S with Se.[16] As can be seen from these examples, although the *ZT* value of SnS has been improved by cation and anion doping, the values obtained by different levels of doping are not very consistent and questions remain regarding the mechanisms involved. This is because there is insufficient structural information on how the dopants are distributed in the SnS crystal, *i.e.*, whether they are a homogeneous, atomic-scale solid solution, segregated, or phase-separated in the form of nanoprecipitates. Thus, the relationship between doping, the structure, and the electronic and thermal transport properties is still not clear.

Another problem, and this is not limited to SnS, is that general methods of fabricating thermoelectric materials require long hours and high temperatures, as described above.[17] On the other hand, wet chemical synthesis offers a shorter and lower-energy approach than the conventional methods of fabricating thermoelectric materials. For instance, we have synthesized various copper chalcogenide-based nanoparticles (NPs) including $Cu_2Sn_{1-x}Zn_xS_3$,[18,19] $Cu_3Zn_{1-x}Al_xSnS_{5-y}$,[20] and $Cu_3Al_{1-x}Ga_xSnS_5$,[21] using a wet chemical synthesis method and then sintered them together to create nanostructured thermoelectric materials with well-defined nanosized grains. The primary advantage of nanostructured thermoelectric materials with such nanosized grains is that size-controlled grain boundaries can be used to effectively scatter long-wavelength phonons without interfering with carrier transport, thereby independently reducing κ_l and improving *ZT*.[18-21] Another important benefit of the wet chemical synthesis method is that it consumes much less energy for thermoelectric material fabrication than conventional methods such as vacuum melting, since it requires only a short time under mild conditions. Several wet chemical synthesis methods for SnS NPs have also been reported,[22-25] although they are few in

number. However, the resulting SnS NPs are often polydisperse and irregularly shaped.[22,23] Some methods for synthesizing monodisperse SnS NPs have been reported,[24,25] but they use highly flammable and toxic reagents such as hexamethyldisilazane or trioctylphosphine.

In this study, we developed a facile, wet chemical synthesis method for relatively monodisperse and spherical SnS NPs, Ag-doped SnS NPs, and Ag-doped $SnS_{1-x}Se_x$ NPs with S partially replaced by Se. These NPs were sintered by hot press, and the relationship between the electronic and thermal transport properties and structure of the sintered pellets – including the influence of grain boundaries, Ag doping, and Se doping – was investigated in detail.

EXPERIMENTAL SECTION

Chemicals

Tin (II) 2-ethylhexanoate [$Sn(Oct)_2$] (purity ≥ 92.5 %), silver nitrate ($AgNO_3$) (99.9999 %), Se powder (99.99%) and oleylamine (OLA) (technical grade, 70 %) were purchased from Sigma-Aldrich. S powder (98.0 %) and toluene (99.0 %) were purchased from Fujifilm Wako. Methanol (99.8 %) and hexane (96.0 %) were purchased from Kanto Chemical. Ethanol was purchased from Nacalai Tesque. Thiourea (TU) (99.0 %) was purchased from Tokyo Chemical Industry. All chemicals were used without further purification.

Synthesis of SnS, SnS:Ag and $SnS_{1-x}Se_x$:Ag NPs

SnS NPs were synthesized with a hot-injection method. Briefly, 60 mmol of $Sn(Oct)_2$ and 125 mL of OLA were put in a 500 mL flask. A stock solution of 30 mmol of S powder and 40 mL of OLA was made in a glass vial by sonication until the S powder dissolved. After 5 min of Ar purging, the solution in the flask was heated up to 180 °C and the stock solution of S powder in OLA was injected into the flask. After the injection, the reaction was allowed to continue for 30 min at a constant temperature of 180 °C. Ar bubbling was constantly applied during the reaction.

After the reaction, the solution was allowed to cool to 100 °C. For the washing of NPs, the reaction solution was divided into nine centrifuge tubes with 20 mL of solution in each. To each tube 10 mL of toluene and 10 mL of methanol were then added, and the tubes were centrifuged at 4,640 × g for 5 min. After discarding the supernatant, 15 mL of toluene was added to each tube to redisperse the precipitate. Then, 25 mL of methanol was added to each tube, which were centrifuged again at 4,640 × g for 5 minutes. After discarding the supernatant, the precipitate was vacuum dried.

In the synthesis of Ag-doped SnS NPs, $AgNO_3$ was added to the stock solution of S dissolved in OLA at different input amounts of Ag ranging from 0.5−2.0 at% with respect to Sn, and the rest was done as in the synthesis of the SnS NPs. Since the highest *ZT* was obtained with 1.5 at% Ag (data on thermoelectric properties of samples with other Ag input ratios are not shown), the input ratio of Ag was fixed at 1.5 at% in this paper. Hereafter, SnS NPs with 1.5 at% Ag will be referred to as SnS:Ag NPs.

In the $SnS_{1-x}Se_x$:Ag NPs synthesis, Se powder was added to the flask at different input amounts of Se ranging from 8−12 at% with respect to S. All other processes were carried out in the same way as the SnS:Ag NPs synthesis.

Ligand Exchange

Because the as-synthesized NPs were capped with OLA, a post-synthesis ligand exchange was performed by replacing OLA with TU, which can be more easily removed from the pellet than OLA during sintering to avoid a harmful effect on the electrical conductivity. Briefly, as a standard condition, 5 g of TU was dissolved in 75 mL of methanol, and this TU solution was added to a dispersion of the NPs (1.6 g) in 25 mL of toluene. The ratio of each chemical was maintained for all ligand exchange reactions of NPs. The mixture was sonicated for 2 h at room temperature. After the ligand exchange reaction, the TU-capped NPs were separated from the solution by

centrifugation and were washed by redispersing in methanol and adding ethanol and hexane. The mixture was centrifuged at 9,060 × g for 15 min and the supernatant was then discarded.

Pelletization

After ligand exchange, NPs were pelletized into a solid disk with a diameter of 10 mm and thickness of 2 mm by hot-press in an Ar atmosphere, at a temperature of 723 K, under a pressure of 300 MPa, and for a sintering of time 5 min. The pellets were polished using silicon carbide abrasive paper (grit size 2000) before characterization. The pellet densities were determined using a gas pycnometer (Shimadzu AccuPyc II 1340).

Characterization

The synthesized NPs were characterized by transmission electron microscopy (TEM, Hitachi H-7650 operated at 100 kV), X-ray diffraction (XRD, Rigaku MiniFlex600 with a Cu Kα source), scanning electron microscopy (SEM, Hitachi TM3030) equipped with an energy-dispersive X-ray spectroscopy (EDS) system, and X-ray photoelectron spectroscopy (XPS, Shimadzu Kratos AXIS-ULTRA DLD) using monochromated Al Kα radiation. The pellets were characterized by XRD and SEM-EDS. The microstructure of the pellets was investigated by a high-angle annular dark field (HAADF) scanning TEM with an EDS system (STEM, Titan G2 80-200, Thermo Fisher Scientific). The STEM specimens were prepared by a standard lift-out method by using a focused ion beam (FIB-SEM, Helios 5UX, Thermo Fisher Scientific). The valence band maxima (VBM) of the pellets were determined by photoemission yield spectroscopy in air (PYSA) (AC-2, Riken Keiki). In PYSA, the sample is scanned using a tunable monochromatic ultraviolet light (4.0–6.2 eV) under ambient conditions, and the number of generated photoelectrons is measured at each excitation energy. The VBM is determined by finding the onset of the PYSA spectra.

Measurement of Thermoelectric Properties

First, κ was measured for the pellets in the out-of-plane direction (parallel to the pressing direction) of the pellet by light flash analysis (LFA467, Netzsch). Using this method, κ ($W \cdot m^{-1} \cdot K^{-1}$) was then calculated using $\kappa = dcD$ where d ($kg \cdot m^{-3}$), c ($J \cdot kg^{-1}\ K^{-1}$), and D ($m^2 \cdot s^{-1}$) are the density, specific heat, and thermal diffusivity of the pellet, respectively. Pellets were then cut into rectangular bars: length, ~ 9 mm; width, ~ 3 mm; height, ~ 2 mm and S and electrical resistivity (ρ) were measured in the in-plane direction (perpendicular to the pressing direction) by a ZEM-3 instrument (Advance Riko). The carrier thermal conductivity, κ_c, was calculated as $\kappa_c = L\sigma T$, where L denotes the Lorentz number ($2.44 \times 10^{-8}\ W \cdot \Omega \cdot K^{-2}$). Finally, κ_l was calculated as $\kappa_l = \kappa - \kappa_c$, and the ZT value was calculated as $ZT = \sigma S^2 T/\kappa$.

Hall Measurements

The Hall voltage V_H (V) was measured at 300 K using a physical properties measurement system (PPMS, Quantum Design) by applying a magnetic field of ±5 T with an alternating current. The electrodes were bonded to the rectangular in-plane specimen using Au sputtering and Au paste. The Hall coefficient, R_H ($cm^3 \cdot C^{-1}$), was calculated using $R_H = V_H d/BI$, where d (m), B (T) and I (A) are the thickness of specimen, external magnetic field and current, respectively. Assuming single carrier transport, n_H (cm^{-3}) and Hall mobility μ_H ($cm^2 \cdot V^{-1} \cdot s^{-1}$) were calculated using $n_H = 1/|R_H|e$ and $\mu_H = R_H\sigma$, where e (C) is the elementary charge.

RESULTS AND DISCUSSION

Structural Analysis of SnS Nanoparticles and Their Sintered Bodies (Pellets)

Figure 1a–c show the TEM images of the as-synthesized SnS NPs; including pristine SnS NPs, SnS:Ag NPs, and $SnS_{0.9}Se_{0.1}$:Ag NPs. TEM images of all other NPs are shown in Figure S1 in the Supporting Information. As can be seen from the TEM images, the size of the SnS NPs is larger than the other doped NPs (77.7 ± 17.9 nm) and they have an uneven surface. In comparison,

SnS:Ag and $SnS_{0.9}Se_{0.1}$:Ag NPs are smaller in size (20.7 ± 5.3 nm for SnS:Ag NPs and 17.2 ± 4.6 nm for $SnS_{0.9}Se_{0.1}$:Ag NPs) and are nearly spherical in shape. The reason why the Ag-doped SnS NPs are smaller in size may be that in the absence of Ag precursors, the SnS NP nucleation rate is slow and crystal growth is dominant resulting in few, large NPs. This is also evidenced by the low reaction yield of SnS NPs (approximately 35%), suggesting that a large amount of unreacted material remains. In contrast, in the case of Ag-doped SnS NPs, the reaction yield was increased (approximately 57%). We believe that because of the high reduction potential of Ag, Ag ions in the reaction solution were first reduced, resulting in the formation of many extremely small Ag nuclei. Subsequently, heterogeneous nucleation of SnS occurred on the surface of the Ag nuclei, resulting in many small SnS:Ag NPs. During the reaction, it is likely that atomic Ag diffuses through the SnS crystal, forming SnS:Ag NPs in which Ag is randomly dispersed at the atomic level. We tried to investigate the spatial distribution of Ag in the SnS:Ag NPs by STEM-EDS mapping, but unfortunately, due to the low Ag doping amount and an unknown effect of contamination in the TEM sample, we could not measure it well. Therefore, the exact spatial distribution of Ag in Ag-doped SnS NPs is unknown. In the case of Se doping, the very similar sizes of the SnS:Ag and $SnS_{0.9}Se_{0.1}$:Ag NPs indicates that there is little effect of Se on NP formation.

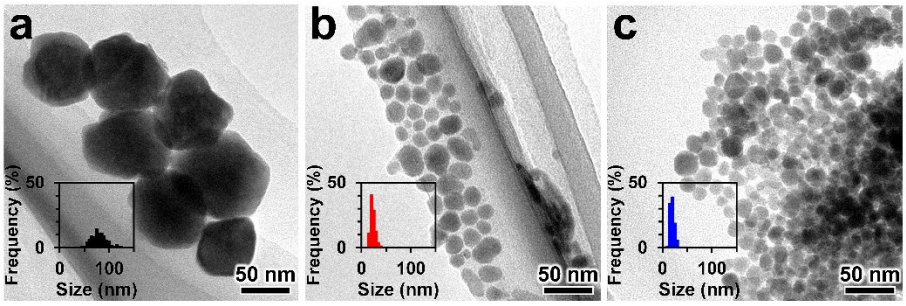

Figure 1. TEM images of (a) SnS, (b) SnS:Ag and (c) $SnS_{0.9}Se_{0.1}$:Ag NPs. The inset in each TEM image is the particle size distribution measured from several randomly-selected TEM images.

Figure 2a and b show the XRD patterns of NPs and pellets of SnS, SnS:Ag and $SnS_{0.9}Se_{0.1}$:Ag. As can be seen from the results, the NPs were all single-phase cubic SnS, which during sintering undergoes a phase transition to the single-phase orthorhombic SnS seen in the pellets. This phase transition occurred because orthorhombic SnS is stable at the sintering temperature.[26] The crystal structures of SnS are shown in Figure S2. It's worth noting that even though orthorhombic SnS has an anisotropic layered structure, the relative powder XRD peak intensities show a good match with the reference patterns. In comparison, powder XRD patterns of orthorhombic SnS pellets by He *et al*. show a very intense peak corresponding to the (0 4 0) plane as a result of the alignment of the crystal structure in this direction.[16] This suggests that the use of spherical, isotropic, cubic phase SnS NPs results in a random orientation of orthorhombic phase grains after sintering, leading to a mostly isotropic orthorhombic SnS pellet. A Williamson-Hall plot based on the NPs XRD pattern was created, as shown in Figure S3, and the results showed that there was no crystal distortion. The mean crystalline sizes, D_{XRD}, were then estimated from the plot to be 30.7 nm for SnS NPs, 18.8 nm for SnS:Ag NPs and 14.7 nm for $SnS_{0.9}Se_{0.1}$:Ag NPs. The D_{XRD} of the NPs decreased in the order of SnS > SnS:Ag > $SnS_{0.9}Se_{0.1}$:Ag, which is consistent with the trend of the average NP size obtained from TEM, D_{TEM}. Comparing D_{TEM} to D_{XRD}, the Ag-doped NPs are found to be almost monocrystalline.

Because the orthorhombic phase of SnS has an intrinsic anisotropy, a Williamson-Hall plot could not be used for the pellets. Therefore, the average value of $\beta_{hkl}\cdot\cos\theta$ for the six peaks with the highest intensities in the 2θ range of 25–40° [the (1 2 0), (0 2 1), (1 0 1), (1 1 1), (0 4 0), and (1 3 1) peaks were used] was calculated, using which D_{XRD} was calculated using the Scherrer formula. Note that β_{hkl} and θ denote the full width at half maximum (FWHM) and the Bragg angle of each

peak. As a result, D_{XRD} was estimated to be 27.2 nm for the SnS pellet, 37.5 nm for the SnS:Ag pellet and 35.4 nm for the $SnS_{0.9}Se_{0.1}$:Ag pellet. For SnS, there was a small reduction in D_{XRD} after sintering, but an increase was observed in the Ag-doped SnS. The small reduction in the SnS pellet was likely due to the variance of the value of β_{hkl} for each peak. However, we can say that there was no significant crystal growth in the SnS pellet during sintering and that the lack of growth in all pellets is likely due to the random orientation of the cubic phase NPs which then form randomly oriented grains in the orthorhombic phase pellets. The values of D_{XRD} for all NPs and all pellet samples are shown in Tables S1 and S2, respectively, in the Supporting Information.

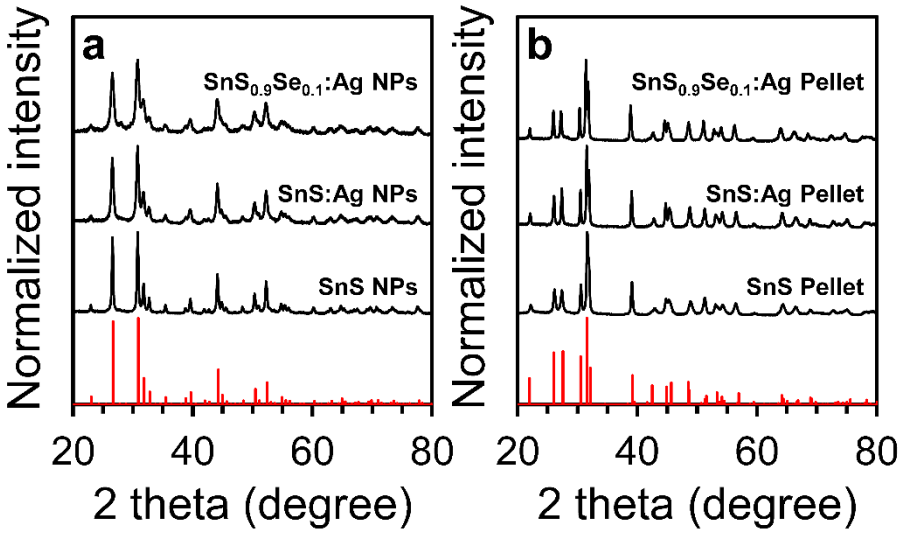

Figure 2. XRD patterns of (a) NPs and (b) pellets. Both figures show the XRD patterns of SnS, SnS:Ag, and $SnS_{0.9}Se_{0.1}$:Ag from bottom to top. Red lines in panels (a) and (b) are reference patterns for cubic and orthorhombic SnS, respectively (PDF Nos. 01-086-9477 and 04-004-3838, respectively).

With Ag and Se doping there was a visible shift of the XRD peaks to lower angles for the pellets (Figure S4), but not for the NPs. Figure S5 shows the lattice constants obtained from the pellet XRD peaks [(1 2 0), (0 2 1), and (0 4 0) peaks were used] plotted against the amount of doping.

The b-axis is represented by the (0 4 0) peak, while – due to the very low intensity of more suitable peaks – the (1 2 0) and (0 2 1) peaks were chosen to approximately represent the a-axis and c-axis, respectively. With Ag doping, only the lattice constant along the a-axis was significantly increased, the reason for which will be discussed later. However, the lattice constants increased in all axial directions when Se was doped. This suggests that Se (ionic radius of Se^{2-} is 1.98 Å) substitutes for S (ionic radius of S^{2-} is 1.84 Å).

The chemical compositions of all NPs and pellets of SnS, SnS:Ag and $SnS_{0.9}Se_{0.1}$:Ag as measured by SEM-EDS are shown in Table S3. In all samples, the Sn:S ratio was almost 1:1 and the composition of the dopants was generally the same as the input molar ratio. STEM-EDS elemental mapping was performed to determine the spatial distribution of dopants in the pellets. Figure 3 shows the HAADF-STEM images and EDS elemental maps for the pellets of SnS:Ag and $SnS_{0.9}Se_{0.1}$:Ag. We can see in the HAADF images how the spherical NPs have become a random arrangement of round grains in the pellet, agreeing with the isotropic nature of the XRD patterns. The EDS results indicate that Ag is segregated into separate regions and thus only a small amount of Ag is incorporated into the SnS crystal at the atomic level. For the SnS:Ag pellet, S was detected in the segregated Ag regions while Sn was not, so the Ag-rich region is likely to be Ag_2S. For the $SnS_{0.9}Se_{0.1}$:Ag pellet, Se was also detected in the Ag-rich region, so the Ag-rich region is likely to be $Ag_2S_{1-x}Se_x$. However, it cannot be said that all Ag-rich regions are exclusively Ag_2S or $Ag_2S_{1-x}Se_x$, and the possibility of the presence of trace amounts of Ag_2O cannot be ruled out. Nevertheless, no Ag_2S- or Ag_2O-derived peaks were observed in the XRD patterns (Figure S6), which is probably due to the extremely small volume fraction of Ag_2S and $Ag_2S_{1-x}Se_x$ (or Ag_2O) regions.

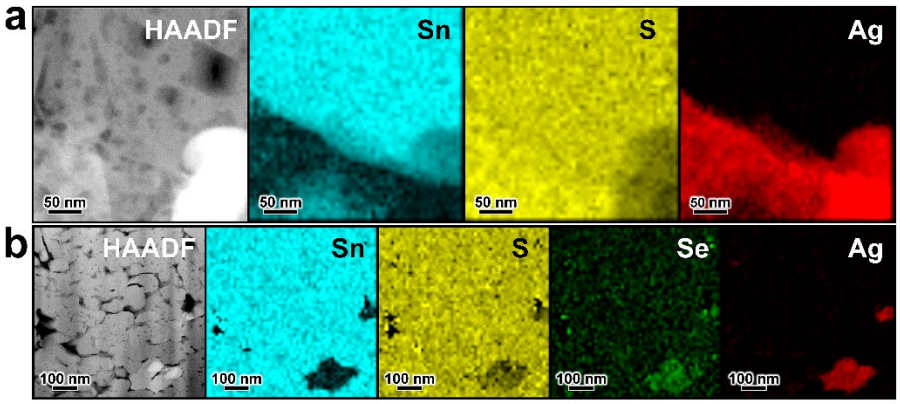

Figure 3. HAADF-STEM images and corresponding EDS elemental maps of pellets of (a) SnS:Ag, and (b) $SnS_{0.9}Se_{0.1}$:Ag. The leftmost grayscale images in (a) and (b) are HAADF-STEM images, and light blue, yellow, green, and red images are EDS elemental maps for Sn (L-line), S (K-line), Se (K-line), and Ag (L-line), respectively.

To investigate the chemical states of the doped Ag and Se, XPS measurements of the pellets were performed. Figure 4a shows the Ag 3d core-level XPS spectrum of the SnS:Ag pellet. The binding energies of the Ag $3d_{5/2}$ and Ag $3d_{3/2}$ spin-orbit pairs are 367.9 eV and 373.9 eV, respectively, suggesting the presence of only Ag^+ (the binding energy of $3d_{5/2}$ for Ag^0 should be on the higher energy side around 368.3 ± 0.1 eV[27,28]). Figure 4b and c show the Ag 3d and Se 3d core-level XPS spectra of the $SnS_{0.9}Se_{0.1}$:Ag pellet, respectively. The binding energies of the Ag $3d_{5/2}$ and Ag $3d_{3/2}$ spin-orbit pairs are 368.0 eV and 374.0 eV, respectively, again indicating the presence of only Ag^+. The Se 3d peak appears as an asymmetric single peak because the energy difference between Se $3d_{5/2}$ and Se $3d_{3/2}$ is only 0.8−0.9 eV. When deconvoluted, the binding energies of the Se $3d_{5/2}$ and Se $3d_{3/2}$ spin-orbit pairs were found to be 53.5eV and 54.4 eV, respectively (Figure 4c). The binding energy of the Se 3d peak in SnSe, which contains Se^{2-}, is reported to be 53.7 eV without peak deconvolution.[29] After deconvolution, the binding energies of the Se $3d_{5/2}$ and Se $3d_{3/2}$ peaks are reported to be 53.7 eV and 54.7 eV, respectively.[30] Therefore this result suggests the presence of Se^{2-} in the $SnS_{0.9}Se_{0.1}$:Ag pellet.

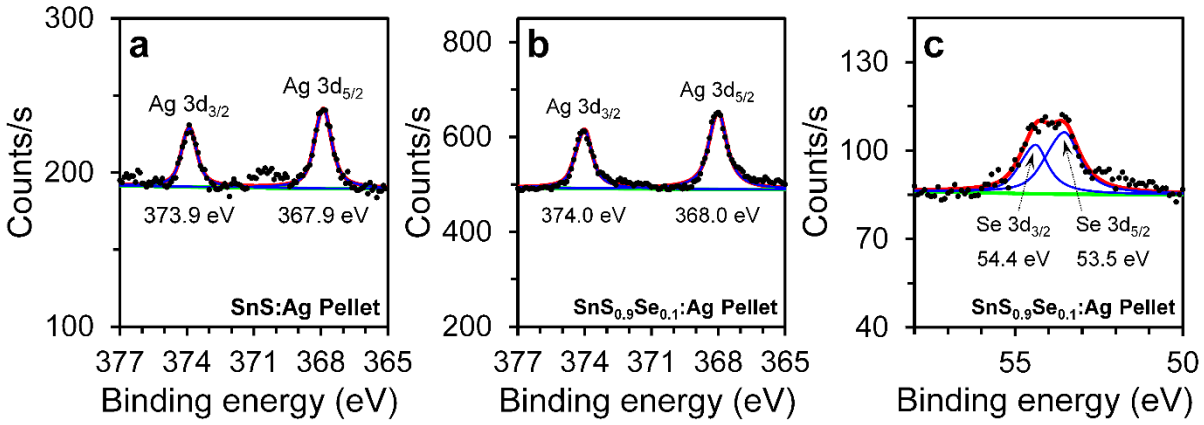

Figure 4. (a) Ag 3d core-level XPS spectrum of the SnS:Ag pellet. (b) Ag 3d and (c) Se 3d core-level XPS spectra of the $SnS_{0.9}Se_{0.1}$:Ag pellet. Black circles, blue lines, red lines, and green lines are the experimentally obtained spectra, the peaks fitted by Voigt function, the sum of the two resolved peaks, and the background, respectively.

Thermoelectric Properties of Pellets (Overview)

Figure 5a–f show the thermoelectric properties of pellets of SnS, SnS:Ag and $SnS_{0.9}Se_{0.1}$:Ag. Figure 5a and b display the temperature dependence of κ and κ_l, respectively. As can be seen from the results, κ_c of all pellets and bulk SnS (control data obtained from Ref. 7) is negligible and κ is dominated by κ_l. The temperature dependence of κ_l for the bulk SnS is proportional to T^{-1} indicating that Umklapp scattering is dominant. In contrast, our pellets show a large reduction in κ_l and a weaker temperature dependence compared to those of the bulk SnS. This indicates that the phonon scattering mechanism in our pellets is strongly affected by defect scattering. We can also see that κ_l is almost the same for pristine SnS and SnS:Ag, but a further reduction of κ_l was observed with Se doping, which may be due to the fact that SnSe has a lower κ_l than SnS.[31]

Looking at the electronic transport properties starting with the Seebeck coefficient, S, we can see that the pristine SnS pellet shows a positive value up to about 600 K, indicating a p-type semiconductor, but above that temperature the sign becomes negative, indicating n-type

semiconduction. Density functional theory (DFT) calculation of an SnS crystal with stoichiometric composition (the calculated band structure is shown in Figure S7 and details of the DFT calculations are given in the SI) revealed that a sign reversal of S occurs at around 550 K, as shown by the dashed line in Figure 5c. Thus, we can infer that our SnS pellet is close to the stoichiometric composition. On the other hand, bulk SnS (Ref. 7) has almost no temperature dependence and no sign reversal. The reason for this is not clarified in Ref. 7, but it is assumed to be due to the nonstoichiometric composition of the bulk SnS. Specifically, it might be a slightly Sn-deficient crystal, in which the Sn vacancies form acceptor levels.[32] Looking at the temperature dependence of S for the SnS:Ag pellet, it is almost the same as that in SnS in the low temperature region, but the decrease in S with increasing temperature is much smaller than in SnS, and no sign reversal occurs (Figure 5c). This may indicate that the SnS:Ag pellet has a larger number of Sn vacancies than the SnS pellet because of the conservation of electrical neutrality of the lattice (a detailed discussion is below), and can thus maintain p-type characteristics over the entire temperature range. The temperature dependence of S in $SnS_{0.9}Se_{0.1}$:Ag shows almost the same behavior as SnS:Ag, but its value is slightly lower than that of SnS:Ag. This may be due to a smaller effective mass m^* and higher n_H in the $SnS_{0.9}Se_{0.1}$:Ag pellet, regarding which a detailed discussion is below. Although a change in band structure is expected for both SnS:Ag and $SnS_{0.9}Se_{0.1}$:Ag, DFT calculations for these materials were not performed because of their complexity and time-consuming nature, making them beyond the scope of this study.

Overall, the values for electrical conductivity, σ, of our pristine SnS pellet are approximately one order of magnitude lower than those of the bulk SnS over the entire measured temperature range as shown in Figure 5d. This is consistent with the hypothesis that the reported bulk SnS is Sn-deficient with additional acceptor levels due to Sn vacancies, compared to our SnS which is

close to its stoichiometric composition, as mentioned above. The values of σ of SnS:Ag are about two orders of magnitude higher than those of our pristine SnS, and are further increased by Se doping. The reasons for the dramatic increase in σ due to Ag and Se doping will be discussed in detail later. As evidenced by the pellet XRD patterns and the HAADF-STEM images of the pellets, we can conclude that the orthorhombic grains in our pellet are randomly oriented resulting in a mostly isotropic nature to all the pellets. This isotropic nature extends to the thermoelectric properties and allows us to combine the electronic and thermal transport properties even though they were measured in different directions. Thus, the significantly increased σ and improved power factor (PF) combine with the reduced κ to produce a marked improvement in the ZT values of SnS:Ag and $SnS_{0.9}Se_{0.1}$:Ag (Figure 5e and f), with maximums of 0.09 (at 666 K) and 0.14 (at 667 K), respectively. This is slightly lower than the other reported ZT values for Ag-doped SnS with 0.5 at% Ag (0.13 at 673 K)[13] and Ag and Se co-doped SnS with 2 at% Ag and 1 at% Se (0.15 around 670 K).[16]

Figure 5g and h show the weighted mobility, μ_w, and thermoelectric quality factor, B,[33] of pellets of SnS, SnS:Ag and $SnS_{0.9}Se_{0.1}$:Ag calculated from S and σ. The temperature dependence of μ_w is quite different for the three pellets of SnS, SnS:Ag, and $SnS_{0.9}Se_{0.1}$:Ag (Figure 5g); SnS has a very low μ_w over the entire temperature range, while SnS:Ag exhibits a dramatically increased μ_w, which is proportional to $T^{-3/2}$ indicating that carrier-phonon scattering is dominant.[33] In the case of $SnS_{0.9}Se_{0.1}$:Ag, μ_w is lower than that of SnS:Ag and the temperature dependence disappears. As a result, B was higher for SnS:Ag than for $SnS_{0.9}Se_{0.1}$:Ag, differing with the trend of ZT (Figure 5h). These results will be discussed in depth later.

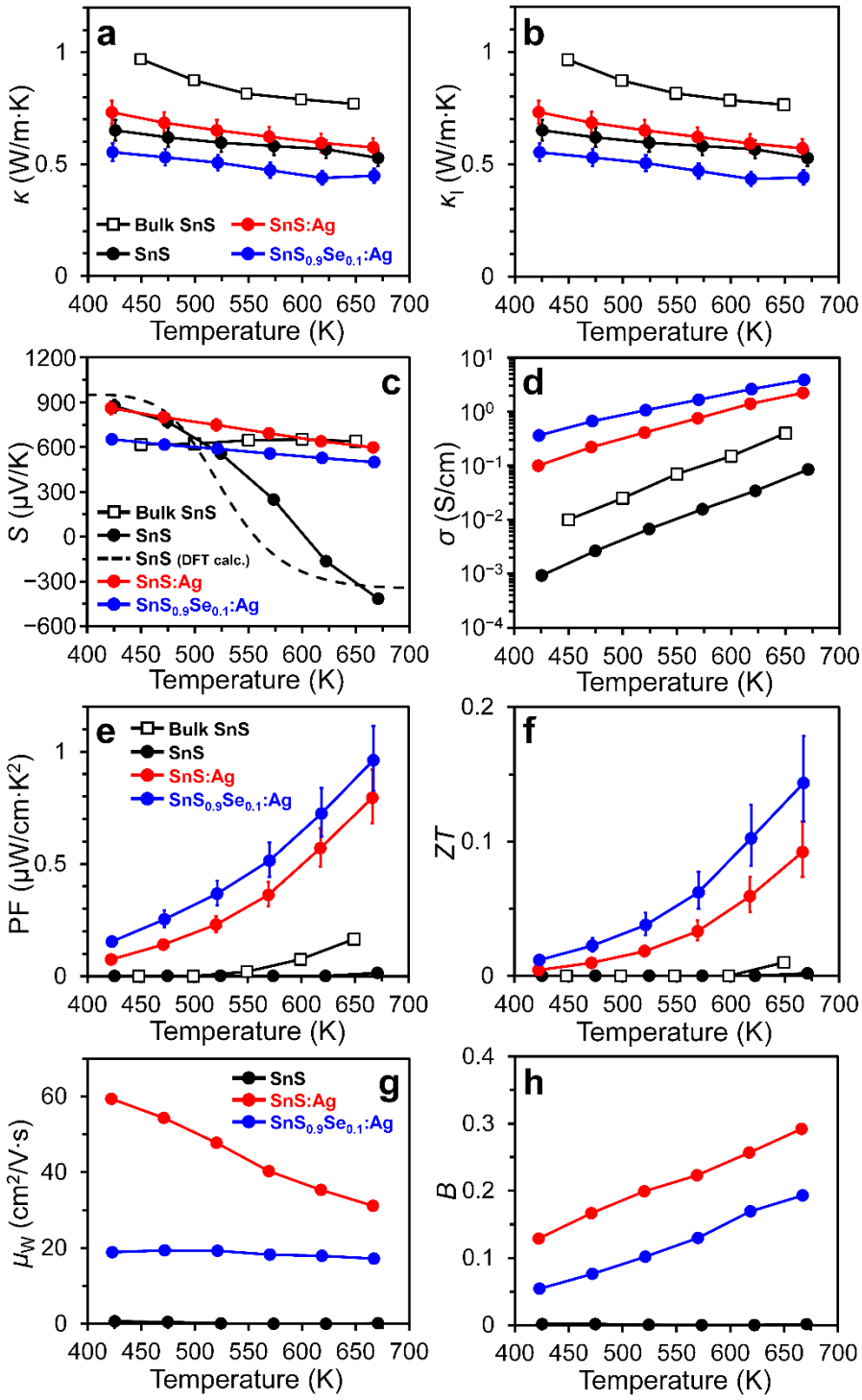

Figure 5. (a) Total thermal conductivity, κ, (b) lattice thermal conductivity, κ_l, (c) Seebeck coefficient, S, (d) electrical conductivity, σ, (e) power factor, PF, (f) dimensionless figure of merit, ZT, (g) weighted mobility, μ_w and (h) thermoelectric quality factor, B for bulk SnS (open squares) (Ref. 7), SnS (black circles), SnS:Ag (red circles), $SnS_{0.9}Se_{0.1}$:Ag (blue circles). The dashed line in panel c is the result of DFT calculation. Note that panels g and h do not include bulk SnS data.

Detailed Discussion of the Electronic Transport Properties

To investigate the cause of the changes in σ due to doping, the activation energy, E_a, for each pellet was estimated using the Arrhenius equation[34]

$$\sigma = \sigma_0 \exp\left(-\frac{E_g}{2k_B T}\right), \quad (1)$$

where $E_g \approx 2E_a$ is the band gap energy, k_B is the Boltzmann constant, and T is the absolute temperature. E_a of SnS, SnS:Ag, and $SnS_{0.9}Se_{0.1}$:Ag were estimated from the Arrhenius plot (Figure 6) to be 0.44, 0.30, and 0.23 eV, respectively. So, for our pristine SnS, E_g is approximately 0.88 eV, which is in close agreement with the reported bandgap energy of bulk SnS.[35,36] This result also suggests that our pristine SnS is a stoichiometric SnS without defects. For SnS:Ag, the E_a value is similar to the reported energy difference between the VBM of a SnS crystal and acceptor levels in the SnS crystal due to Sn vacancies (0.22 eV).[37]

In the previous structural analysis, we saw that there are two forms of Ag in SnS:Ag. One is in the form of segregated nanoprecipitates (Ag_2S), and the other is in the form of Ag ions intercalated between the layers of SnS. Ag^+ intercalation likely causes the creation of Sn vacancies to maintain electrical neutrality. Since the interlayer distance of SnS is 4.3 Å,[38] Ag^+ (ionic radius: 1.26 Å) can intercalate readily. In addition, if Sn^{2+} were to be substituted by Ag^+, Sn vacancies are unlikely to form. In the identically-structured SnSe the number density of Sn vacancies can be controlled by annealing temperature, and a low number density of Sn vacancies has been reported to correspond to a reduction in the volume of the unit cell.[39] This means that a high number density of Sn vacancies will cause an increase in the unit cell volume and the lattice constants. This is thought

to be due to the stronger repulsion between neighboring anions when Sn vacancies are formed. In the structural analysis section, we noted that only the lattice constant in the a-axis direction was significantly increased by Ag doping (see Figure S5). Due to the accordion-like crystal structure of SnS, we can say Sn vacancies are more likely to cause an increase in the flexible a-axis compared to the relatively rigid c-axis. The lack of change in the b-axis is thought to be because of the fact that the van der Waals gap (approximately 4.3 Å) is sufficiently larger than the ionic radius of Ag^+ (1.26 Å), resulting in no change in the lattice constant even when Ag ions are inserted between the layers. Thus, we can conclude that the decrease in activation energy in SnS:Ag samples is due to the intercalation of Ag^+ ions increasing the number of Sn vacancies which lead to the formation of acceptor levels in the band structure. However, when the Ag input ratio is above 0.5 at%, there is no change in the lattice constant in the a-axis direction, suggesting that the amount of intercalated Ag^+ in the orthorhombic SnS crystal is extremely small and the solubility limit is below 0.5 at%. Therefore, when the amount of Ag exceeds 0.5 at%, the excess is not intercalated and we believe instead forms Ag_2S or $Ag_2S_{1-x}Se_x$ nanoprecipitates.

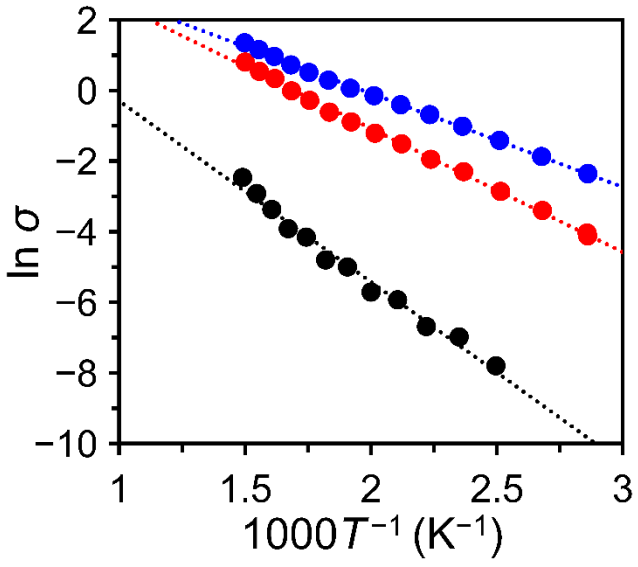

Figure 6. Natural logarithmic plot of electrical conductivity, ln σ, with respect to the reciprocal of temperature for pellets of SnS (black circles), SnS:Ag (red circles), and $SnS_{0.9}Se_{0.1}$:Ag (blue circles).

For $SnS_{0.9}Se_{0.1}$:Ag, E_a (0.23 eV) was found to be slightly lower than that of SnS:Ag. The E_a of $SnS_{1-x}Se_x$ has been reported to be about 0.12−0.24 eV,[40,41] depending on composition and crystal orientation, which is smaller than that of SnS:Ag (approximately 0.3 eV). The VBM of the pellets was determined by PYSA and was found to be about 5.3 eV for all pellets of SnS, SnS:Ag, and $SnS_{0.9}Se_{0.1}$:Ag, with no significant difference (Figure S8). So, we can conclude that the lower E_a for $SnS_{0.9}Se_{0.1}$:Ag is due to a reduction in the Sn vacancy acceptor level energy as a result of Se doping.

The structural analysis and the Arrhenius plot of electrical conductivity strongly suggest that Ag doping causes the formation of Sn vacancy acceptor levels. Therefore, we performed Hall measurements on the SnS, SnS:Ag, and $SnS_{0.9}Se_{0.1}$:Ag pellets at 300 K to estimate the n_H and the μ_H. The values of n_H at 300 K were determined to be 2.1×10^{15}, 6.7×10^{15}, and 34.9×10^{15} cm^{-3} for SnS, SnS:Ag, and $SnS_{0.9}Se_{0.1}$:Ag, respectively, so n_H increases with Ag doping and further increases with Se doping, corresponding to the observed changes in E_a. It has also been reported that the conduction band minimum (CBM) of SnS is decreased by the formation of a solid solution with Se.[42] In other words, the inclusion of Se in $SnS_{0.9}Se_{0.1}$:Ag results in a smaller band gap than SnS:Ag, and the increase in interband excitation may be one of the reasons for the increase in n_H. We also noted that the VBMs of SnS:Ag and $SnS_{0.9}Se_{0.1}$:Ag are comparable to the VBM of Ag_2S (5.3 eV),[43] so energy filtering effects are unlikely to be observed.

The values of μ_H were calculated to be 2.1, 11.8, and 5.5 $cm^2 \cdot V^{-1} \cdot s^{-1}$ for SnS, SnS:Ag, and $SnS_{0.9}Se_{0.1}$:Ag, respectively. The electrical resistivity values (ρ) for all pellets at 300 K used for the calculation are shown in Table S4 in the Supporting Information. SnS:Ag showed the highest μ_H, while $SnS_{0.9}Se_{0.1}$:Ag showed a μ_H value lower than SnS:Ag and higher than pristine SnS. To explore the reasons for these changes, a Pisarenko plot (shown in Figure 7) was created to estimate the m^* of each sample assuming that acoustic phonon scattering is dominant for SnS:Ag ($\mu_w \propto T^{-3/2}$, see Figure 5g) and neutral impurity scattering is dominant for $SnS_{0.9}Se_{0.1}$:Ag ($\mu_w \propto T^0$, see Figure 5g). Note that in the case of pristine SnS, the electrical resistance is too high at 300 K to make the ZEM-3 measurements reliable, so the DFT calculated value of S at 300 K was used in the Pisarenko plot. Because the relation between μ_H and m^* can be given as[44]

$$\mu_H = \frac{e\tau}{m^*}, \tag{2}$$

where τ denotes the charge carrier relaxation time, the values of τ were also calculated for all pellets. The values of m^* and τ for all pellets are listed in Table S5. As can be seen in Figure 7 and Table S5, both m^* and τ of SnS:Ag are larger than those of SnS. However, for $SnS_{0.9}Se_{0.1}$:Ag, both values lie between those of SnS:Ag, and SnS. Although the reason for the increase in m^* for SnS:Ag and $SnS_{0.9}Se_{0.1}$:Ag over the m^* for SnS is not clear, a previous study has reported an increase in the density-of-states effective mass of $Bi_{2-x+a}Sb_xTe_{3-b}$ solid solutions as a result of nanostructuring or when SiO_2 fine particles are incorporated into the matrix as nanoinclusions.[45] Therefore, the increase in m^* for SnS:Ag and $SnS_{0.9}Se_{0.1}$:Ag may be due to Ag_2S and $Ag_2S_{1-x}Se_x$ nanoprecipitates. In the case of τ, since intercalated Ag^+ formed Sn vacancies, and since Ag^+ has a lower hole scattering ability than Sn^{2+}, the ionized impurity scattering effect may have been suppressed, resulting in an overall increase in τ. As for the difference between SnS:Ag and $SnS_{0.9}Se_{0.1}$:Ag,

since the m^* of SnSe is known to be smaller than that of SnS,[46] it can be expected that the m^* of $SnS_{0.9}Se_{0.1}$:Ag is smaller than that of SnS:Ag. Additionally, the impurity scattering effect due to the substitution of S with Se may have resulted in $SnS_{0.9}Se_{0.1}$:Ag having a smaller τ than SnS:Ag. We can consider the above discussion to be valid because the VBM of each pellet obtained by PYSA, as mentioned above, is comparable to the VBM of Ag_2S or $Ag_2S_{1-x}Se_x$, ruling out energy filtering effects. This is also supported by the temperature dependence of μ_w (Figure 5g), which is proportional to $T^{-3/2}$ in the case of SnS:Ag and is thus dominated by carrier-phonon scattering, whereas the temperature dependence disappears in $SnS_{0.9}Se_{0.1}$:Ag and neutral impurity scattering dominates.

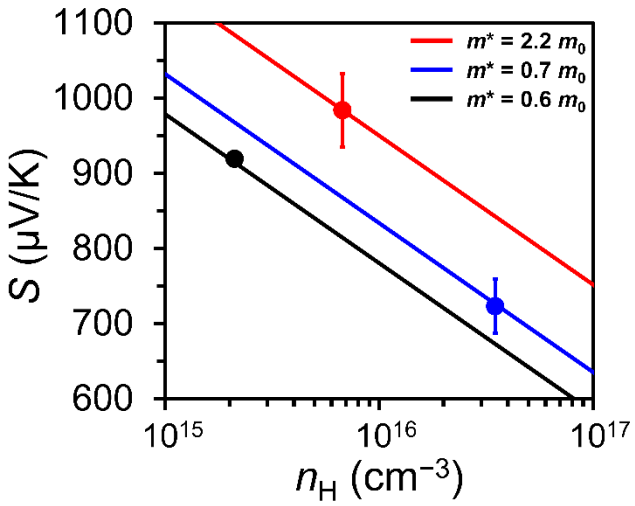

Figure 7. Pisarenko plot for various values of effective mass m^*, where m_0 is the mass of the free electron. The black circle and line represent SnS, red circle and line represent SnS:Ag, and blue circle and line represent $SnS_{0.9}Se_{0.1}$:Ag.

The relationship between the drift mobility, μ, and μ_w is expressed by the following equation:[33]

$$\mu_w \cong \mu \left(\frac{m^*}{m_0}\right)^{3/2}, \quad (3)$$

Using this equation, we can estimate the values of μ_w using the values of m^* obtained by our Pisarenko plot and the measured μ_H at 300 K, giving values of μ_w at 300 K of approximately 38.5 $cm^2 \cdot V^{-1} \cdot s^{-1}$ and 3.2 $cm^2 \cdot V^{-1} \cdot s^{-1}$ for SnS:Ag and $SnS_{0.9}Se_{0.1}$:Ag, respectively. The calculated values of μ_w obtained from the experimentally obtained data of S and σ were 59.4 $cm^2 \cdot V^{-1} \cdot s^{-1}$ and 18.9 $cm^2 \cdot V^{-1} \cdot s^{-}1$ at 423 K for SnS:Ag and $SnS_{0.9}Se_{0.1}$:Ag, respectively. Considering the difference in temperature and the difference between μ_H and μ, the estimated values seem reasonable. Note that due to the high electrical resistivity of the SnS sample below 400 K, a reliable ZEM-3 measurement could not be obtained, and so an accurate low temperature μ_w could not be calculated.

Finally, the reason why the B value was higher for SnS:Ag than $SnS_{0.9}Se_{0.1}$:Ag (Figure 5h) can be explained by looking at the equation used to calculate B.[33]

$$B = \left(\frac{k_B}{e}\right)^2 \frac{8\pi e(2m_0 k_B T)^{3/2}}{3h^3} \frac{\mu_w}{\kappa_l} T, \quad (4)$$

where e is the electron charge and h is the Planck constant. In $SnS_{0.9}Se_{0.1}$:Ag an increase in carrier density compared to SnS:Ag leads to an improvement in σ and PF, however μ_w is reduced due to the increase in neutral impurity scattering. As seen in Eq. (4), B is proportional to μ_w/κ_l which is the cause of the reduction in B even as ZT is seen to increase by 1.6 times (Figure 5f).

CONCLUSIONS

We developed a facile wet chemical synthesis method for tin monosulfide (SnS) nanoparticles (NPs), which are expected to be an environmentally benign thermoelectric material, and furthermore, demonstrated the ease of Ag and Se doping. The thermoelectric properties of pellets obtained by sintering the synthesized NPs were investigated, and a significant decrease in the

lattice thermal conductivity, κ_l, due to nanostructuring and a remarkable increase in the electrical conductivity, σ, due to Ag and Se doping were found. As a result, *ZT* was improved to 0.09 at 666 K for Ag-doped SnS with 1.5 at% Ag (SnS:Ag) and to 0.14 at 667 K for $SnS_{0.9}Se_{0.1}$:Ag, which is more than 10 times higher than the *ZT* of bulk SnS and comparable to the reported Ag and Se co-doped SnS. Furthermore, we were able to explain the contributions of the two dopants, Ag and Se, to the thermoelectric properties in terms of their distribution in the crystal structure. Detailed investigation of the electronic transport properties for SnS:Ag indicated that the significant improvement in *ZT* is due to the presence of intercalated Ag^+, which increased the carrier density by encouraging the formation of Sn vacancies, and the carrier mobility due to increased relaxation time. In the case of $SnS_{0.9}Se_{0.1}$:Ag, the carrier mobility was lower than that of SnS:Ag due to neutral impurity scattering (alloy scattering) as Se partially replaced S, but the further increase in carrier density due to the change in band structure resulted in a higher electrical conductivity than SnS:Ag, which coupled with a reduction in κ_l resulted in a *ZT* that is 1.6 times higher than that of SnS:Ag at 667K. The results of this study provide important insight and understanding into the electrical and thermal transport properties of the layered material SnS.

ASSOCIATED CONTENT

The following files are available free of charge.

TEM images of other NPs (other than SnS, SnS:Ag, and $SnS_{0.9}Se_{0.1}$:Ag) not shown in the main text, crystal structures of SnS, the Williamson-Hall plot of NPs, magnified XRD patterns of pellets, dependence of lattice constants of pellets on Ag and Se doping amounts, *E*-*k* relation of orthorhombic phase of SnS, PYSA spectra of pellets, mean crystalline sizes of other NPs and pellets, compositions of NPs and pellets of SnS, SnS:Ag and $SnS_{0.9}Se_{0.1}$:Ag, electrical resistivity, effective mass and charge carrier relaxation time of all pellets, and details of the DFT calculation method can be found in the supporting information.

AUTHOR INFORMATION

Corresponding Author

***Shinya Maenosono** − School of Materials Science, Japan Advanced Institute of Science and Technology, 1-1 Asahidai, Nomi, Ishikawa 923-1292, Japan; E-mail: shinya@jaist.ac.jp

Authors

Keiji Kobayashi − School of Materials Science, Japan Advanced Institute of Science and Technology, 1-1 Asahidai, Nomi, Ishikawa 923-1292, Japan

Mari Takahashi − School of Materials Science, Japan Advanced Institute of Science and Technology, 1-1 Asahidai, Nomi, Ishikawa 923-1292, Japan

Simon Moore − School of Materials Science, Japan Advanced Institute of Science and Technology, 1-1 Asahidai, Nomi, Ishikawa 923-1292, Japan

Masanobu Miyata − School of Materials Science, Japan Advanced Institute of Science and Technology, 1-1 Asahidai, Nomi, Ishikawa 923-1292, Japan

Philipp Sauerschnig − Global Zero Emission Research Center, National Institute of Advanced Industrial Science and Technology (AIST), Tsukuba, Ibaraki 305-8568, Japan

Jun Uzuhashi − Research Center for Magnetic and Spintronic Materials, National Institute for Materials Science (NIMS), 1-2-1 Sengen, Tsukuba, Ibaraki 305-0047, Japan

Michihiro Ohta − Global Zero Emission Research Center, National Institute of Advanced Industrial Science and Technology (AIST), Tsukuba, Ibaraki 305-8568, Japan

Tadakatsu Ohkubo − Research Center for Magnetic and Spintronic Materials, National Institute for Materials Science (NIMS), 1-2-1 Sengen, Tsukuba, Ibaraki 305-0047, Japan

Author Contributions

The work was initiated by S.Ma. (Shinya Maenosono); K.K., S.Mo. (Simon Moore), M.T. and S.Ma. devised the method; K.K. and S.Mo. constructed the experimental setup and performed all the experiments under the supervision of M.T., M.M., and S.Ma.; M.M. performed the DFT calculation; P.S. measured thermoelectric properties of pellets under the supervision of M.O.; J.U. conducted STEM observation of pellets under the supervision of T.O.; K.K., M.T. and S.Ma. drafted the manuscript. All authors reviewed the manuscript and have given approval to the final version of the manuscript.

Funding Sources

This work was supported by JSPS KAKENHI (Grant Number 19H02440) and the Thermal and Electric Energy Technology Foundation.

Notes

The authors declare no competing financial interest.

ACKNOWLEDGMENT

This work was supported by JSPS KAKENHI under Grant No. 19H02440. This work was partially supported by the Thermal & Electric Energy Technology Foundation.

REFERENCES

1. Banai, R. E.; Horn, M. W.; Brownson, J. R. S. A Review of Tin (II) Monosulfide and Its Potential as a Photovoltaic Absorber. *Sol. Energy Mater. Sol. Cells* **2016**, *150*, 112–129.

2. Zhang, H.; Man, B.; Zhang, Q. Topological Crystalline Insulator SnTe/Si Vertical Heterostructure Photodetectors for High-Performance Near-Infrared Detection. *ACS Appl. Mater. Interfaces* **2017**, *9*, 14067–14077.

3. Shen, Y.; Zhang, Y.; Huo, J.; Li, X.; Yan, Z.; Pan, Y.; Sun, W.; Deng, N.; Kang, W. Two-Dimensional SnSe Material for Solar Cells and Rechargeable Batteries. *J. Energy Storage* **2023**, *69*, 107958.

4. Zhao, L.-D.; Lo, S.-H.; Zhang, Y.; Sun, H.; Tan, G.; Uher, C.; Wolverton, C.; Dravid, V. P.; Kanatzidis, M. G. Ultralow Thermal Conductivity and High Thermoelectric Figure of Merit in SnSe Crystals. *Nature* **2014**, *508*, 373–377.

5. Zhang, X.; Zhao, L.-D. Thermoelectric Materials: Energy Conversion Between Heat and Electricity. *J. Materiomics* **2015**, *1*, 92–105.

6. Sun, F.-H.; Li, H.; Tan, J.; Zhao, L.; Wang, X.; Hu, H.; Wang, C.; Mori, T. Review of Current $ZT > 1$ Thermoelectric Sulfides. *J. Materiomics* **2024**, *10*, 218–233.

7. Asfandiyar; Cai, B.; Zhao, L.-D.; Li, J.-F. High Thermoelectric Figure of Merit ZT > 1 in SnS Polycrystals. *J. Materiomics* **2020**, *6*, 77–85.

8. Wang, L.; Chang, S.; Zheng, S.; Fang, T.; Cui, W.; Bai, P.-P.; Yue, L.; Chen, Z.-G. Thermoelectric Performance of Se/Cd Codoped SnTe via Microwave Solvothermal Method. *ACS Appl. Mater. Interfaces* **2017**, *9*, 22612–22619.

9. Liu, D.; Wang, D.; Hong, T.; Wang, Z.; Wang, Y.; Qin, Y.; Su, L.; Yang, T.; Gao, X.; Ge, Z.; Qin, B.; Zhao, L.-D. Lattice Plainification Advances Highly Effective SnSe Crystalline Thermoelectrics. *Science* **2023**, *380*, 841–846.

10. Zhou, C.; Lee, Y. K.; Yu, Y.; Byun, S.; Luo, Z.-Z.; Lee, H.; Ge, B.; Lee, Y.-L.; Chen, X.; Lee, J. Y.; Cojocaru-Mirédin, O.; Chang, H.; Im, J.; Cho, S.-P. Wuttig, M.; Dravid, V. P.; Kanatzidis, M. G.; Chung, I. Polycrystalline SnSe with A Thermoelectric Figure of Merit Greater Than The Single Crystal. *Nat. Mater.* **2021**, *20*, 1378–1384.

11. Pathak, R.; Sarkar, D.; Biswas, K. Enhanced Band Convergence and Ultra-Low Thermal Conductivity Lead to High Thermoelectric Performance in SnTe. *Angew. Chem. Int. Ed.* **2021**, *60*, 17686–17692.

12. Ibáñez, M.; Hasler, R.; Genç, A.; Liu, Y.; Kuster, B.; Schuster, M.; Dobrozhan, O.; Cadavid, D.; Arbiol, J.; Cabot, A.; Kovalenko, M. V. Ligand-Mediated Band Engineering in Bottom-Up Assembled SnTe Nanocomposites for Thermoelectric Energy Conversion. *J. Am. Chem. Soc.* **2019**, *141*, 8025–8029.

13. Tan, Q.; Zhao, L.-D.; Li, J.-F.; Wu, C.-F.; Wei, T.-R.; Xing, Z.-B.; Kanatzidis, M. G. Thermoelectrics with Earth Abundant Elements: Low Thermal Conductivity and High Thermopower in Doped SnS. *J. Mater. Chem. A* **2014**, *2*, 17302–17306.

14. Zhou, B.; Li, S.; Li, W.; Li, J.; Zhang, X.; Lin, S.; Chen, Z.; Pei, Y. Thermoelectric Properties of SnS with Na-Doping. *ACS Appl. Mater. Interfaces* **2017**, *9*, 34033–34041.

15. He, W.; Wang, D.; Wu, H.; Xiao, Y.; Zhang, Y.; He, D.; Feng, Y.; Hao, Y.-J.; Dong, J.-F.; Chetty, R.; Hao, L.; Chen, D.; Qin, J.; Yang, Q.; Li, X.; Song, J.-M.; Zhu, Y.; Xu, W.; Niu, C.; Li, X.; Wang, G.; Liu, C.; Ohta, M.; Pennycook, S. J.; He, J.; Li, J.-F.; Zhao, L.-D. High Thermoelectric Performance in Low-Cost $SnS_{0.91}Se_{0.09}$ Crystals. *Science* **2019**, *365*, 1418–1424.

16. He, Z.; Zhu, J.; Su, W.; An, X.; Zhao, C.; Yuan, W.; Lin, L.; Ang, R. Achieving High Quality Factor and Enhanced Thermoelectric Performance in Polycrystalline SnS by Ag Doping and Se Alloying. *Appl. Phys. Lett.* **2023**, *123*, 242104.

17. d'Angelo, M.; Galassi, C.; Lecis, N. Thermoelectric Materials and Applications: A Review. *Energies* **2023**, *16*, 6409.

18. Zhou, W.; Shijimaya, C.; Takahashi, M.; Miyata, M.; Mott, D.; Koyano, M.; Ohta, M.; Akatsuka, T.; Ono, H.; Maenosono, S. Sustainable Thermoelectric Materials Fabricated by Using $Cu_2Sn_{1-x}Zn_xS_3$ Nanoparticles as Building Blocks. *Appl. Phys. Lett.* **2017**, *111*, 263105.

19. Zhou, W.; Dwivedi, P.; Shijimaya, C.; Ito, M.; Higashimine, K.; Nakada, T.; Takahashi, M.; Mott, D.; Miyata, M.; Ohta, M.; Miwa, H.; Akatsuka, T.; Maenosono, S. Enhancement of the Thermoelectric Figure of Merit in Blended $Cu_2Sn_{1-x}Zn_xS_3$ Nanobulk Materials. *ACS Appl. Nano Mater.* **2018**, *1*, 4819–4827.

20. Dwivedi, P.; Miyata, M.; Higashimine, K.; Takahashi, M.; Ohta, M.; Kubota, K.; Takida, H.; Akatsuka, T.; Maenosono, S. Nanobulk Thermoelectric Materials Fabricated from Chemically Synthesized $Cu_3Zn_{1-x}Al_xSnS_{5-y}$ Nanocrystals. *ACS Omega* **2019**, *4*, 16402–16408.

21. Dwivedi, P.; Miyata, M.; Higashimine, K.; Takahashi, M.; Zhou, W.; Ohta, M.; Maenosono, S. Effect of Gallium Substitution in $Cu_3Al_{1-x}Ga_xSnS_5$ Nanobulk Materials on Thermoelectric Properties. *ACS Appl. Energy Mater.* **2020**, *3*, 5784–5791.

22. Rana, C.; Bera, S. R.; Saha, S. Growth of SnS Nanoparticles and Its Ability as Ethanol Gas Sensor. *J. Mater. Sci. Mater. Electron.* **2019**, *30*, 2016–2029.

23. Hegde, S. S.; Murahari, P.; Fernandes, B. J.; Venkatesh, R.; Ramesh, K. Synthesis, Thermal Stability and Structural Transition of Cubic SnS Nanoparticles. *J. Alloys Compd.* **2020**, *820*, 153116.

24. Huang, P.-C.; Huang, J.-L.; Wang, S.-C.; Shaikh, M. O.; Lin, C.-Y. Photoelectrochemical Properties of Orthorhombic and Metastable Phase SnS Nanocrystals Synthesized by a Facile Colloidal Method. *Thin Solid Films* **2015**, *596*, 135–139.

25. Hickey, S. G.; Waurisch, C.; Rellinghaus, B.; Eychmüller, A. Size and Shape Control of Colloidally Synthesized IV-VI Nanoparticulate Tin(II) Sulfide. *J. Am. Chem. Soc.* **2008**, *130*, 14978–14980.

26. Lindwall, G.; Shang, S.; Kelly, N. R.; Anderson, T.; Liu, Z.-K. Thermodynamics of The S–Sn System: Implication for Synthesis of Earth Abundant Photovoltaic Absorber Materials. *Sol. Energy* **2016**, *125*, 314–323.

27. Lützenkirchen-Hecht, D.; Strehblow, H.-H. Anodic Silver (II) Oxides Investigated by Combined Electrochemistry, Ex Situ XPS and In Situ X-ray Absorption Spectroscopy. *Surf. Interface Anal.* **2009**, *41*, 820–829.

28. Maenosono, S.; Lee, J.-D.; Dao, A. T. N.; Mott, D. Peak Shape Analysis of Ag 3d Core-Level X-ray Photoelectron Spectra of Au@Ag Core-Shell Nanoparticles Using an Asymmetric Gaussian–Lorentzian Mixed Function. *Surf. Interface Anal.* **2012**, *44*, 1611–1614.

29. Shalvoy, R. B.; Fisher, G. B.; Stiles, P. J. Bond Ionicity and Structural Stability of Some Average-Valence-Five Materials Studied by X-ray Photoemission. *Phys. Rev. B* **1977**, *15*, 1680–1697.

30. Athithya, S.; Mohamed Jibri, K. P.; Harish, S.; Hayakawa, K.; Kubota, Y.; Ikeda, H.; Hayakawa, Y.; Navaneethan, M.; Archana, J. Probing an Enhanced Anisotropy Seebeck Coefficient and Low Thermal Conductivity in Polycrystalline Al Doped SnSe Nanostructure. *AIP Adv.* **2023**, *13*, 015311.

31. Rundle, J.; Leoni, S. Layered Tin Chalcogenides SnS and SnSe: Lattice Thermal Conductivity Benchmarks and Thermoelectric Figure of Merit. *J. Phys. Chem. C* **2022**, 126, 14036–14046.

32. Vidal, J.; Lany, S.; d'Avezac, M.; Zunger, A.; Zakutayev, A.; Francis, J.; Tate, J. Band-Structure, Optical Properties, and Defect Physics of the Photovoltaic Semiconductor SnS. *Appl. Phys. Lett.* **2012**, *100*, 032104.

33. Snyder, G. J.; Snyder, A. H.; Wood, M.; Gurunathan, R.; Snyder, B. H.; Niu, C. Weighted Mobility. *Adv. Mater.* **2020**, *32*, 2001537.

34. Warnes, L. A. A. *Electronic Materials*; Springer: Boston, USA, 1990; pp 84–117.

35. Ettema, A. R. H. F.; de Groot, R. A.; Haas, C.; Turner, T. S. Electronic structure of SnS deduced from photoelectron spectra and band-structure calculations. *Phys. Rev. B* **1992**, *46*, 7363.

36. Reddy, K. T. R.; Reddy, N. K.; Miles, R. W. Photovoltaic Properties of SnS Based Solar Cells. *Sol. Energy Mater. Sol. Cells* **2006**, *90*, 3041–3046.

37. Reghima, M.; Akkari, A.; Guasch, C.; Kamoun-Turki, N. Structural, Optical, and Electrical Properties of SnS:Ag Thin Films. *J. Electron. Mater.* **2015**, *44*, 4392–4399.

38. Zhou, T.; Pang, W. K.; Zhang, C.; Yang, J.; Chen, Z.; Liu, H. K.; Guo, Z. Enhanced Sodium-Ion Battery Performance by Structural Phase Transition from Two-Dimensional Hexagonal-SnS_2 to Orthorhombic-SnS. *ACS Nano* **2014**, *8*, 8323–8333.

39. Sraitrova, K.; Cizek, J.; Holy, V.; Plechacek, T.; Benes, L.; Jarosova, M.; Kucek, V.; Drasar, C. Vacancies in SnSe Single Crystals in a Near-Equilibrium State. *Phys. Rev. B* **2019**, *99*, 035306.

40. Patel, K.; Solanki, G.; Patel, K.; Pathak, V.; Chauhan, P. Investigation of Optical, Electrical and Optoelectronic Properties of SnSe Crystals. *Eur. Phys. J. B* **2019**, *92*, 200.

41. Jethwa, V. P.; Patel, K.; Pathak, V. M.; Solanki, G. K. Enhanced Electrical and Optoelectronic Performance of SnS Crystal by Se Doping. *J. Alloys Compd.* **2021**, *883*, 160941.

42. Im, H. S.; Myung, Y.; Cho, Y. J.; Kim, C. H.; Kim, H. S.; Back, S. H.; Jung, C. S.; Jang, D. M.; Lim, Y. R.; Park, J.; Ahn, J.-P. Facile Phase and Composition Tuned Synthesis of Tin Chalcogenide Nanocrystals. *RSC Adv.* **2013**, *3*, 10349–10354.

43. Pang, M.; Hu, J.; Zeng, H. C. Synthesis, Morphological Control, and Antibacterial Properties of Hollow/Solid Ag_2S/Ag Heterodimers. *J. Am. Chem. Soc.* **2010**, *132*, 10771–10785.

44. *Thermoelectrics: Design and Materials*, 1st ed.; Lee, H. S., Ed.; Wiley: Chichester, UK, 2017; pp 206–229.

45. Lukyanova, L. N.; Shabaldin, A. A.; Samunin, A. Y.; Usov, O. A. Effective Mass, Mobility of Charge Carriers, and Lattice Thermal Conductivity in Nanocomposite Thermoelectrics Based on Bismuth and Antimony Chalcogenides. *Semiconductors* **2022**, *56*, 10–13.

46. Guo, R.; Wang, X.; Kuang, Y.; Huang, B. First-Principles Study of Anisotropic Thermoelectric Transport Properties of IV-VI Semiconductor Compounds SnSe and SnS. *Phys. Rev. B* **2015**, *92*, 115202.